

High-Contrast Coronagraph Performance in the Presence of Focal Plane Mask Defects

*Erkin Sidick, Stuart Shaklan, Kunjithapatham Balasubramanian, and Eric Cady
Jet Propulsion Laboratory, California Institute of Technology, 4800 Oak Grove Drive, Pasadena,
CA 91109, USA

ABSTRACT

We have carried out a study of the performance of high-contrast coronagraphs in the presence of mask defects. We have considered the effects of opaque and dielectric particles of various dimensions, as well as systematic mask fabrication errors and the limitations of material properties in creating dark holes. We employ sequential deformable mirrors to compensate for phase and amplitude errors, and show the limitations of this approach in the presence of coronagraph image-mask defects.

Key words: Coronagraphy, adaptive optics, high-contrast imaging, space telescopes, exoplanets

1. INTRODUCTION

This paper presents both simulated and measured results on the sensitivity of broadband contrast to the defects of an occulting mask in a Lyot coronagraph implemented on the High-Contrast Imaging Testbed (HCIT) at NASA's Jet Propulsion Laboratory (JPL). This testbed is the Exoplanet Exploration Program's primary platform for experimentation [1-3]. It is used to provide laboratory validation of key technologies as well as demonstration of a flight-traceable approach to implementation. It employs a 48x48 actuator deformable-mirror (DM) and a broadband wavefront correction algorithm called Electric Field Conjugation (EFC) to obtain the required 10^{-10} contrast [4]. In an effort to be able to predict the measured contrast performance of the coronagraph, we have investigated the following defects of the occulting mask: randomly distributed opaque spots on the occulter, occulters with asymmetric optical-density (OD) profiles, and occulter profile with reduced OD peak. We have also carried out simulations by using the measured microscope image of an occulter's transmittance while keeping its phase the same as that of the model, as well as adding some phase values to the measured occulter spots. The laboratory testing was carried out with either a 2%-narrowband or a 10%-broadband light. The simulations were conducted with MACOS (Modeling and Analysis for Controlled Optical Systems) [5], and their results were compared with measurements. We achieved good agreement between the measurement and the simulation in some of the cases investigated. In three earlier papers we reported on the broadband contrast sensitivity of the number and position of dead actuators, beam walk due to translation of a flat optic in the beam, as well as on the effects of occulter displacement, an opaque spot on the occulter, and the controlled dark-hole dimensions[6-8].

2. DEFINITION OF DARK-HOLE AREA AND MEASURED CONTRAST MAPS

The detailed background information of the Lyot coronagraph used in this study is given in Ref. [7] and is not repeated here. For the current optical system with only one DM, we carry out wavefront control (WFC) over a region Ω_b , where Ω_b is a D-shaped dark-hole region bound by $X \geq X_{\min}$ and $R \leq R_{\max}$, with $X = x/f$, $Y = y/f$, $R = \sqrt{X^2 + Y^2}$, x and y are the horizontal and the vertical position variables on the corresponding image-plane, and f is the focal length. In this paper we used $[X_{\min}, R_{\max}] = [3.5 \ 11]\lambda/D$ for Ω_b . We evaluate the performance of the HCIT using the normalized intensity,

$$I_n(x, y) = I(x, y) / I_0, \quad (1)$$

*Erkin.Sidick@jpl.nasa.gov; Phone 1 818 393-7585; Fax 1 818 393-3290; www.jpl.nasa.gov

where $I(x, y)$ is the image intensity of the occulted star, and I_0 is the maximum value of the un-occulted star intensity. We keep track of I_b , the mean value of $I_n(x, y)$ inside a “Big” region Ω_b defined above.

3. MEASURED CONTRAST RESULTS

The main goal of this paper is to find an explanation for the measured normalized intensity floor observed in an HCIT experiment carried out in the spring of 2013. The measured data, which is the total residual light in the dark hole, is shown in Fig. 1(a) while the estimated coherent parts of the intensity are shown in Fig. 1(b). Each of these plots shows $I_n(x, y)$ maps measured using 5 different bandpass filters each with a passband of 2%, and their mean normalized intensity value, as indicated in the figure. The rightmost mean intensity map corresponds to the 10%-broadband contrast. The top-row is the intensity map measured directly with the science camera first then normalized by the unocculted intensity peak when the 5 bands are equally weighted. The bottom-row shows the estimated coherent part of the intensity; this is the part that responds to multiple probe intensity measurements [4] created by setting the DM to 4 preset phases. The top-row, which is the total measured signal, corresponds to the combination of the coherent and the incoherent light, and the bottom one to the estimate of the coherent light only. In the next section, we compare our simulated $I_n(x, y)$ maps with those shown in Fig. 1(b).

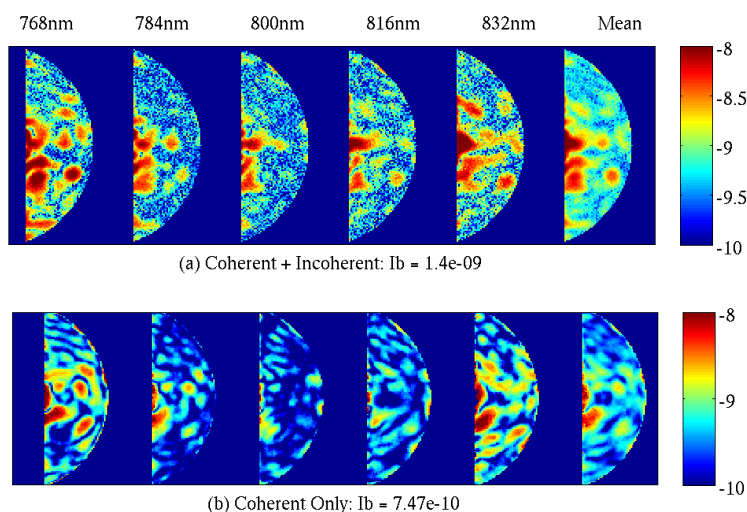


Figure 1. Measured $I_n(x, y)$ maps at 5 individual wavelengths listed at the figure title and their mean. The mean $I_n(x, y)$ corresponds to a 10%-broadband contrast map. (a) Coherent plus incoherent parts. (b) Coherent part only.

4. SIMULATED RESULTS

In this section, we present the results of simulated contrast maps corresponding to a nominal case as well as the several cases of occulter defects, and compare them with the measured intensity maps in Fig. 1(b).

The HCIT uses a modified one-dimensional band-limited occulter whose OD profile at wavelength $\lambda = 800\text{nm}$ is truncated and smoothed by convolution with a Gaussian function. This smoothed pattern is described in detail in Refs. [9-10]. Specifically, the sinc² intensity transmission profile is $T_{\text{sinc}}(x) = \{1 - [\sin(\pi x/w)/(\pi x/w)]^2\}^2$, $\text{OD}_{\text{sinc}}(x) = -\log_{10} T_{\text{sinc}}(x)$, with $w = 142\mu\text{m}$. The truncation and smoothing gives $\text{OD}_{\text{rel}}(x) = \min[\text{OD}_{\text{sinc}}(x), 8] \otimes G(x)$ with $G(x) = (2\pi\sigma^2)^{-1/2} \exp[-x^2/(2\sigma^2)]$, where $\sigma = 9\mu\text{m}$. For practical reasons, the maximum transmission is often less than unity, so the final transmission is $T(x) = T_0 10^{-\text{OD}_{\text{rel}}(x)}$, for some maximum transmission T_0 . The two OD profiles, OD_{sinc} and OD_{rel} , are shown graphically in Fig. 2(a). The spatially-varying transmission profile is optically realized by spatially varying the thicknesses of Ni layers deposited on a fused quartz substrate. Because Ni has a large index of refraction ($n \sim 2.5$ at 800nm), regions of the occulter with higher OD (lower transmission, thicker Ni) also have a greater optical path length in transmission than low OD regions. The spatially-varying transmitted E-field is therefore complex-valued. In addition to the spatial variations in OD and phase, the OD and phase also vary with wavelength. Ni was chosen for this application because its OD and phase are less dispersive than other practical materials, as described in Ref. [11]. We

include the dispersion of both occulter OD and phase in our simulations. The profile of the occulter phase at $\lambda=800\text{nm}$, $\phi(800)$ is also shown in Fig. 2(a) in radians. Figure 2(b) shows the OD dispersion at five wavelength values relative to that at $\lambda=800\text{nm}$. The occulter phase dispersion is weaker than the OD dispersion, and the $\phi(\lambda) - \phi(800)$ has the largest value of -0.012 radians at the center of occulter and at $\lambda = 768\text{nm}$. For this occulter, $T(x) = 0.5$ at $x/f = 3.3\lambda/D$, where $D = 48\text{mm}$ is the diameter of the system clear aperture and f is the focal length. The front end F-number (F/#) of this optical system is 31.25.

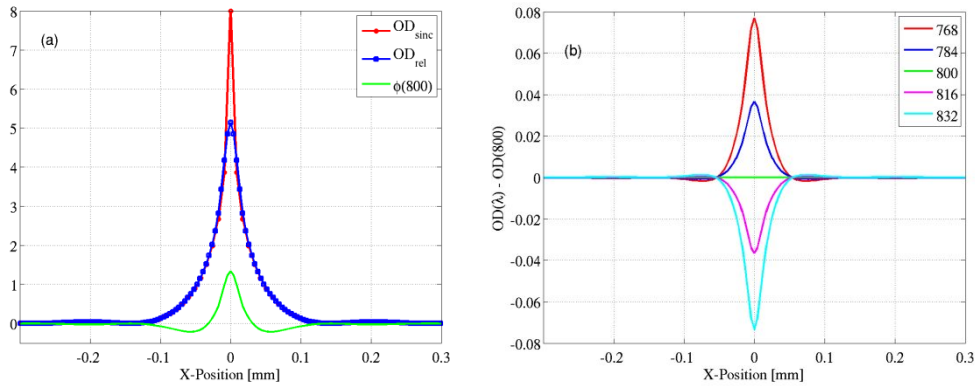


Figure 2. (a) The x-profiles of occulter Optical Densities, OD_{sinc} and OD_{rel} , as well as transmitted occulter phase at $\lambda = 800\text{nm}$, $\phi(800)$, where the latter is given in radians. (b) Occulter OD dispersion, where the figure legend shows five wavelength values in nm. These parameters correspond to a linear-sinc² occulting mask consisting of Ni deposited on a fused quartz substrate. The OD_{rel} corresponds to the OD of the occulter used on the testbed.

4.1 Nominal Case

As a base-line, we carried out a set of broadband wavefront-control (WFC) simulations using the nominal, modeled transmission coefficient and phase-delay of the occulter. In the experiment, the phase error at the system exit pupil was flattened by iterative phase estimation and DM adjustments before the dark-hole was generated. Therefore, in our simulations, we did not include the surface height errors of the various optics. Thus, the only error affecting the contrast of the current system is the parasitic phase-delay of the occulting mask. This phase was not accounted for in the mask design, though later generations of masks do take this into account [9]. Figures 3(a) and 3(b) are the 10%-broadband (760-840 nm) $I_n(x, y)$ maps before and after control, respectively. They are the full-view of the normalized PSFs

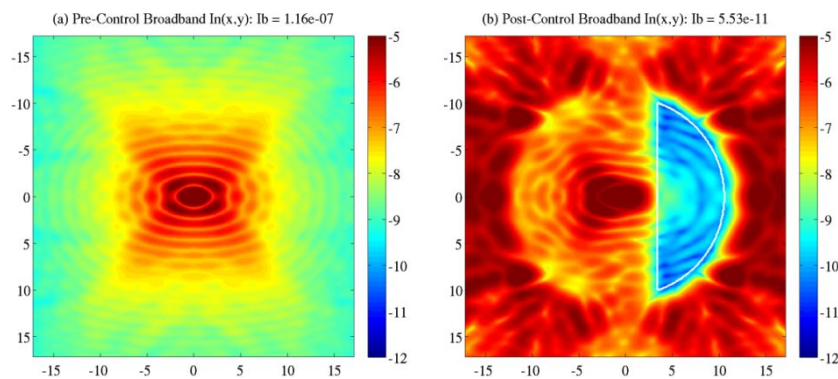


Figure 3. Normalized intensities, $I_n(x, y)$, of the nominal case. (a) Before control, and (b) after control. The units of the x- and the y-axes are λ/D .

inside a $30 \times 30 \lambda/D$ square area. The post-control $I_n(x, y)$ maps are shown in Figs. 4(a) and 4(b) in the same form as the measured data in Figs. 1(a-b), where the only difference between the top and the bottom rows is the color-stretch.

The fine features of the $I_n(x, y)$ maps in Figs. 4 are quite different from that of the Fig. 1(b), and the simulated broadband contrast ($I_b = 5.53e^{-11}$) is more than an order of magnitude better than the measured data ($I_b = 7.47e^{-10}$). In spite of the residual occulter phase, the EFC algorithm was able to converge to an intensity level well below the minimum level experienced in the laboratory. The efficiency of the broadband WFC process is shown in Fig. 5(a), where I_b is shown as a function of control iteration. The final actuator commands yielding the present post-control results are shown in Fig. 5(b). The small discontinuity in the I_b versus control-iteration curve took place when we changed the actuator regularization factor from 0.1 to 1.0 after 10 control iterations.

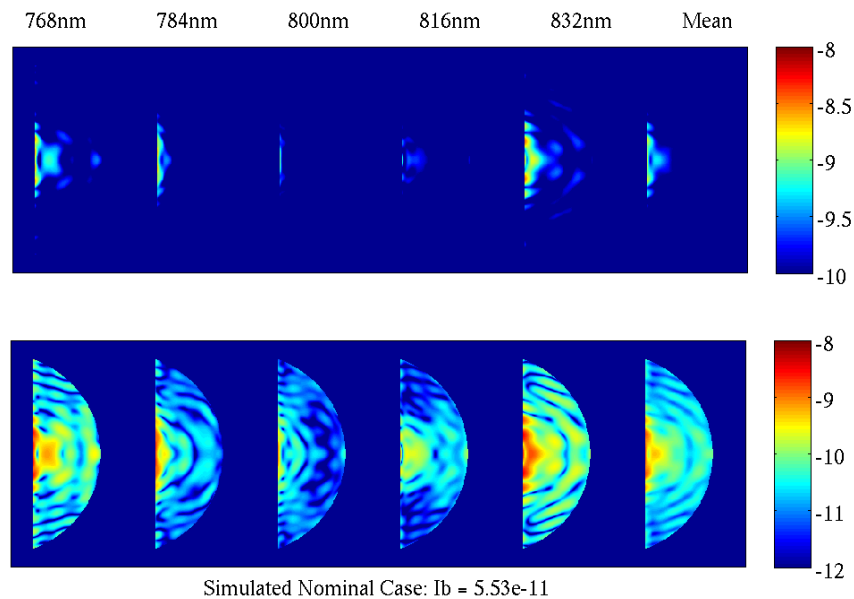


Figure 4. Post-control normalized intensities, $I_n(x, y)$, of the nominal case. The top- and the bottom-rows show the same data plotted with different color-stretches.

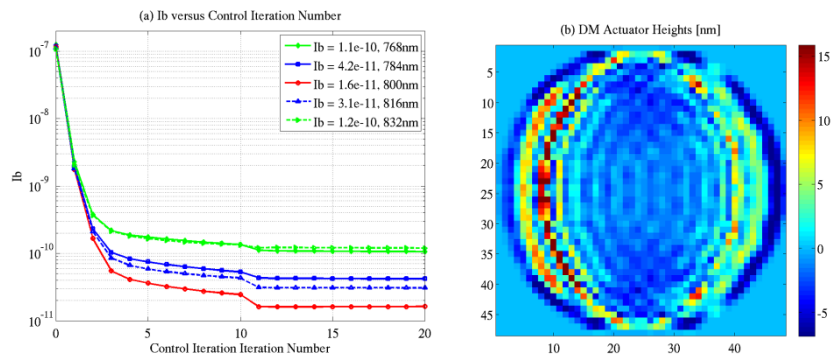


Figure 5. (a) Normalized mean intensity, I_b , versus control iteration number. The five curves correspond to 5 different individual wavelengths indicated in the figure legend. The I_b -values at the end of 20 control iterations are also listed in the figure legend. The discontinuity after 10 control iterations took place when the actuator regularization factor is increased from 0.1 to 1.0. (b) DM actuator heights obtained at the end of 20 WFC iterations as shown in part (a).

4.2 Opaque Particles

Next, we introduced 140 opaque, square-shaped particles randomly distributed inside an annular region bounded by 2 to $12\lambda/D$ on the occulter surface as shown in Fig. 6. We assumed the particles would alter only the transmission amplitude of the occulter, making it equal to zero at positions where the particles are located. We considered two values for

particle widths, 2.8 and 2.0 μm , and obtained the after-control $I_n(x, y)$ maps shown in Figs. 7(a) and 7(b), respectively. The measured I_b value (Fig. 1(b)) fell in between the two values of the current simulations. The morphology of the $I_n(x, y)$ map in Fig. 7(b) is somewhat comparable to Fig. 1(b); given equal weighting of each wavelength band, the contrast was best in the central band and worst at the extrema. This is an indicator, though by no means proof, that the measured coherent contrast maps of Fig. 1(b) is caused by opaque spots on the occulter. For this case, we did not carry out an exhaustive search for opaque spots whose distribution on the occulter surface would give rise to the contrast maps observed in Fig. 1(b), for reasons to be explained later in this paper.

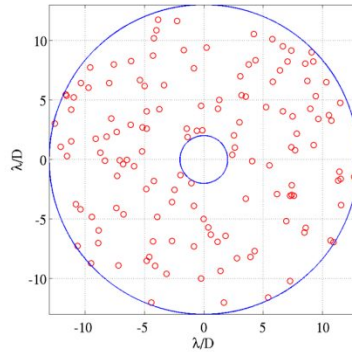


Figure 6. Locations of 140 particles randomly distributed inside an annular region bounded by 2 to 12 λ/D on the occulter surface.

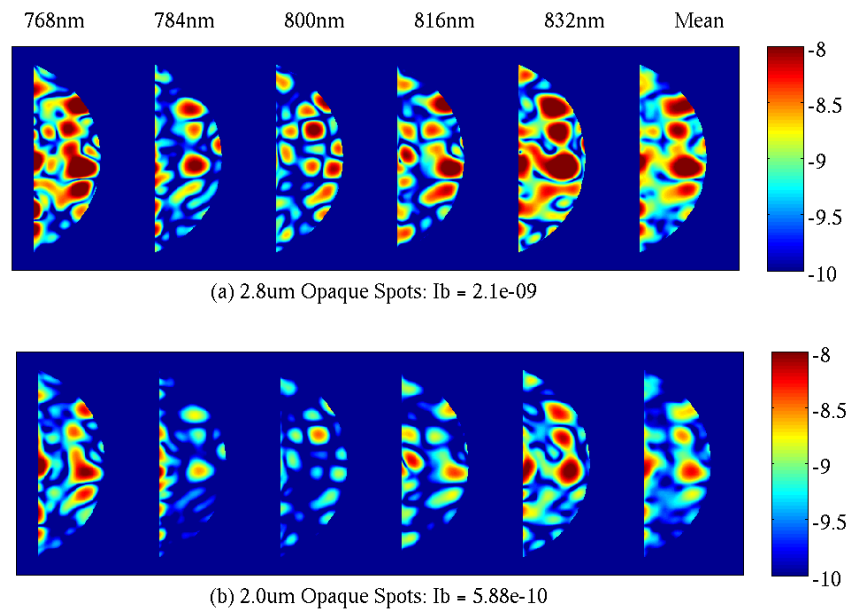


Figure 7. Post-control normalized intensities, $I_n(x, y)$. Top: 140 opaque, square spots with $a = 2.8\mu\text{m}$ (width) were introduced to occulter transmission amplitude. The phase-delay of the occulter is kept the same. Bottom: Same as Top except $a = 2.0\mu\text{m}$.

4.3 Asymmetric and Reduced OD

In this sub-section, we introduced the following types of distortions to the occulter OD profile: (1) In a region where $x \geq 0$ and $OD_{\text{max}} \geq OD \geq 1$, where $OD_{\text{max}} = 5.1378$, we reduced the OD values linearly as

$$OD' = 0.6042 \times OD + 0.3958 \quad (1)$$

such that the peak of the new OD , or OD' , is 3.5. In a region where $x < 0$ and $OD > 3.5$, we truncated the OD values to 3.5. This case is shown graphically in Fig. 8(a). The phase versus OD relationship is kept the same as before, that is, when the OD value is reduced, the phase value is also adjusted according to the original phase versus OD relationship. (2) In a region where $OD > 1$, we symmetrically reduced the OD values linearly using Eqn. (1) so that the peak of the new OD , or OD' , is 3.5. This is shown graphically in Fig. 8(b). The occulter phase is treated in the same way as in the previous case. (3) The OD profile is skewed to the left as compared to the nominal case, which also led to some reduction of the OD peak, as shown in Fig. 8(c). The occulter phase profile is also skewed in the same way as OD . This is done in the following way: Assume the 1-D OD profile is given by $od = f(n_v)$, where $n_v = -512, -511, \dots, 511$ is an 1×1024 pix array. Now we construct a new array,

$$n_v' = \text{sign}(n_v - n_0) \times \sqrt{(n_v - n_0)^2 + n_v^2} / \sqrt{2} \quad (2)$$

and map $f(n_v)$ onto n_v' by 1-D interpolation, where $\text{sign}(x) = -1$ when $x < 0$ and $\text{sign}(x) = 1$ when $x > 0$. In Fig. 8(c), we used $n_0 = -5.5$. Figures 9(a-c) show the $I_n(x, y)$ maps corresponding to the above 3 types of occulter OD errors. The I_b values worsen as compared to the nominal case as expected, but are still much better than the measured one. Also, the regularly-spaced Airy-rings are preserved in all 3 cases to some levels, resulting in $I_n(x, y)$ morphology that does not match with the measured data. That is, these types of occulter errors cannot explain the observed contrast behavior of the current system.

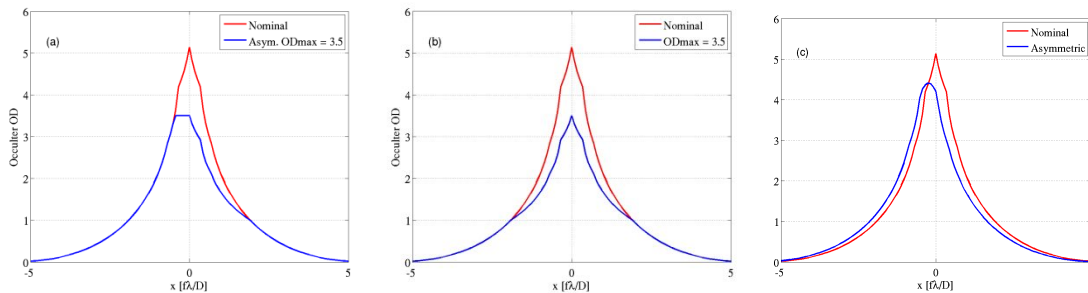


Figure 8. Occulter OD x-profiles versus x-position. (a) Occulter with asymmetric and reduced OD_{\max} profile. (b) Occulter with reduced OD_{\max} profile. (c) Occulter with skewed OD profile.

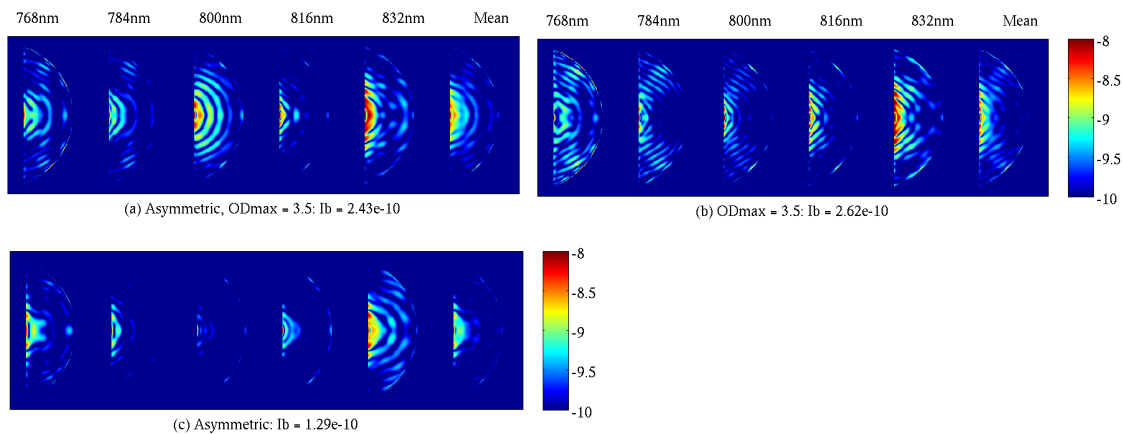


Figure 9. After-control normalized intensities corresponding to the blue-curves in Figs. 8(a-c).

4.4 Increased Occulter Phase

We also examined a case where the occulter phase is doubled everywhere as compared to the nominal case, as shown in Fig 10(a), where the red-curve shows the nominal phase at $\lambda = 800\text{nm}$ and the blue one is equal to $2x$ of that. We do not

know of a physical phenomenon that would cause such a large phase dependence, but differences between the catalog values of the bulk material properties and the applied thin film could lead to a similar, though smaller phenomenon. The corresponding $I_n(x, y)$ results are shown in Fig. 10(b). The $I_n(x, y)$ maps exhibit features that are very different from those of the measured data in this case; that is, a large central lobe and a bright secondary lobe near the outer part of the dark hole dominate the residual light. The residual intensity due to a proportional phase error does not resemble the coherent scatter in the experiment (Fig. 1(b)).

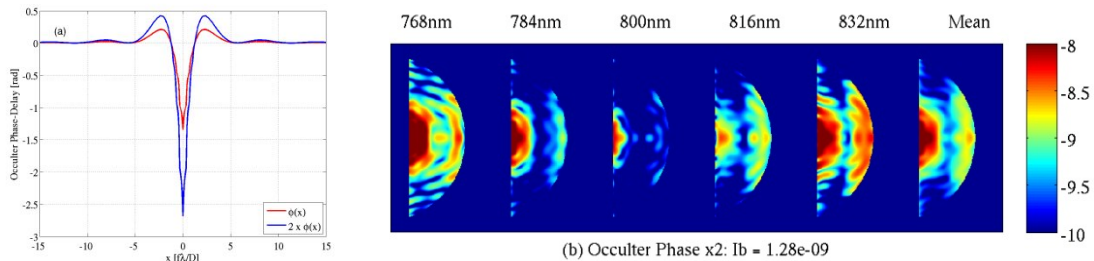


Figure 10. (a) Occluder phase-delay at $\lambda = 800\text{nm}$. (b) After-control normalized intensities corresponding to the blue-curve in part (a).

4.5 Using Measured Occluder Transmission Images

The speckly nature of the observed coherent dark hole floor, and the simple particle distribution model that produces a similar result, indicate that localized mask errors are the likely cause of the contrast floor. We have measured the transmission (amplitude only, not phase) of the occluder using high resolution (10x magnification, $0.97\mu\text{m}$ resolution) microscope images to inform a model and see if a mask characterization can be used to predict dark hole contrast. Figure 11(a) is the transmission image of the front side of the occluder with the mask written on it. The back side of the 2 mm thick substrate is not in focus using the $\text{NA} = 0.3$ objective. This is the composite of 10 images taken to average local fringing and detector noise. The vertical red-line is at $x = 3.5f\lambda/D$, the red-circle has a radius of $r = 10f\lambda/D$; this image roughly corresponds to the area of the occluder used in our experiments. We also took 10 images of the back side of the occluder, averaged them to obtain a single image, and multiplied the resulting image with Fig. 11(a) to obtain a “composite-image” of the front and the back sides of the occluder shown in Fig. 11(b). The HCIT optical system F-

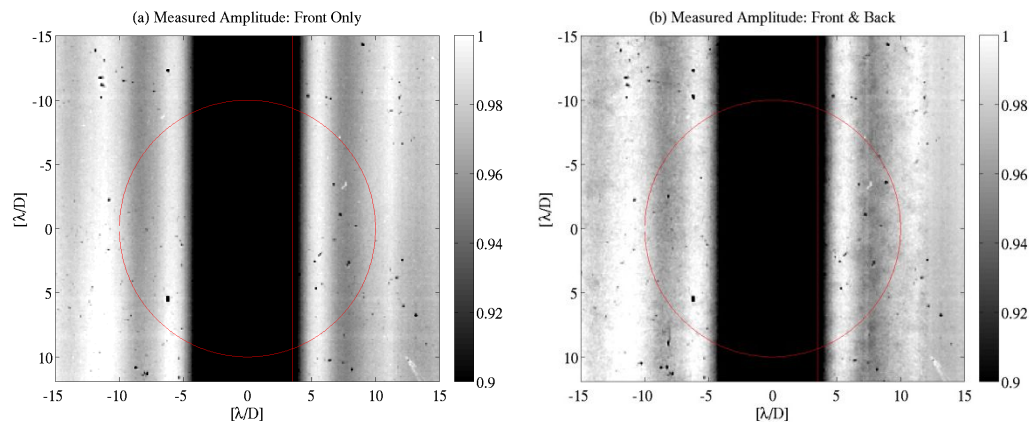


Figure 11. Transmitted amplitude images of the occluder. (a) Front (occluder) side only. (b) Combined image of the front and the back sides.

number at the occluder plane is 31.25, so the E-field changes very little when the beam propagates through the occluder glass. Thus, to a good approximation, the composite image in Fig. 11(b) can be used to account for the spots on both the front and the back sides of the occluder glass without modeling the propagation through the substrate. The microscope used in this measurement does not have enough dynamic range to measure the transmittance of the central dark area of the occluder. Therefore, we replaced the transmittance of the central $\sim 4\lambda/D$ -wide area with the model data forming a

composite model. Figure 12 is an example of the x-profiles of the occulter amplitude function. The red- and the blue-curves correspond to the original and composite data, respectively, and the green dashed-curve is the as-designed mask model. In the plot, 1pixel corresponds to $2.1\mu\text{m}$. We used the modeled data for the occulter phase and its dispersion for both the corresponding to the measured and composite OD.

Figures 13(a) and 13(b) are the after-control $I_n(x, y)$ maps obtained with the occulter amplitude function shown in Figs. 11(a) and 11(b), respectively. The dark hole floor is $\sim 3\times$ below the measured floor. We have repeated these simulations for different areas of the occulter (moving along the central lobe in Fig. 11), but failed to achieve a result that matches both qualitatively and quantitatively the measured data. That is, the fine-features of the $I_n(x, y)$ maps are not quite similar to those of the measured data, and the I_b values of the simulations are several times better than the measured one.

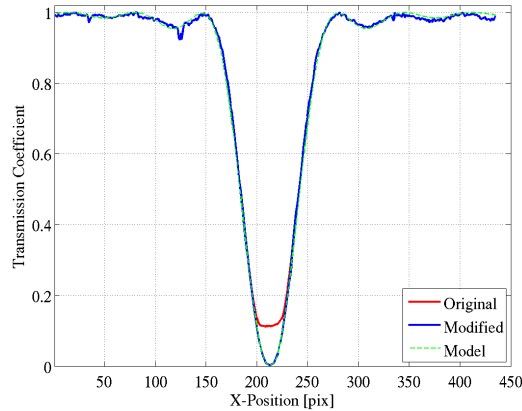


Figure 12. An example of the x-profile of the occulter transmission. The red- and the blue-curves correspond to the original and the modified measured data, and green dashed-curve is the model.

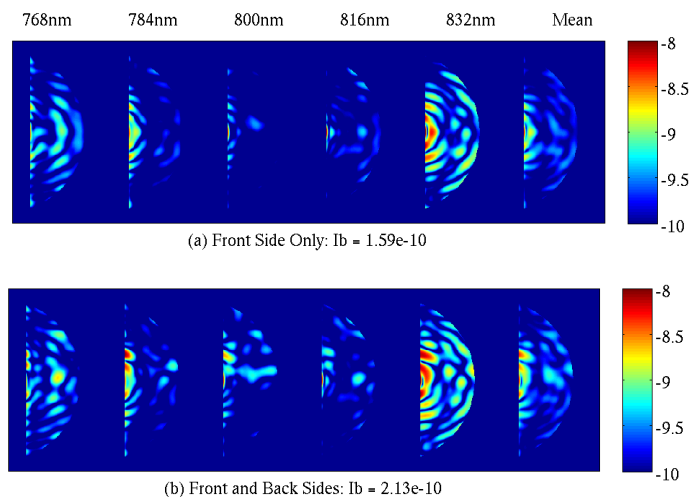


Figure 13. After-control normalized intensities obtained using the two occulter images in Figs. 11(a) and 11(b), respectively.

4.6 Adding Phase to Measured Occulter Spots

As noted above, we were able to measure the amplitude transmission, but not the phase, through the mask. We have artificially added phase to the spots to test the importance of phase and to motivate characterization by other means. Figure 14 is a surface plot of the measured optical density of the dark-hole side of the occulter surface after removing the

linear-sinc² occulter pattern. The x- and the y-axes are in units of λ/D , and the z-axis is OD. In this plot, the original OD value is multiplied by 50 for the sake of better visibility.

We have added additional phase to the occulter transmission function in the form of $\phi_{\text{spot}} \approx \pi \times F_{\text{spot}} \text{OD}_{\text{spot}}$. Where F_{spot} is a multiplier we tested at values 0, 0.25, 0.5, 0.75, and 1. At or near the optical resolution limit of the microscope objective, quantitative measure of the transmitted intensity through small spots / particulates is subject to large errors. Phase measurements by non contact methods with standard interferometers is also subject to large errors at the resolution of interest.

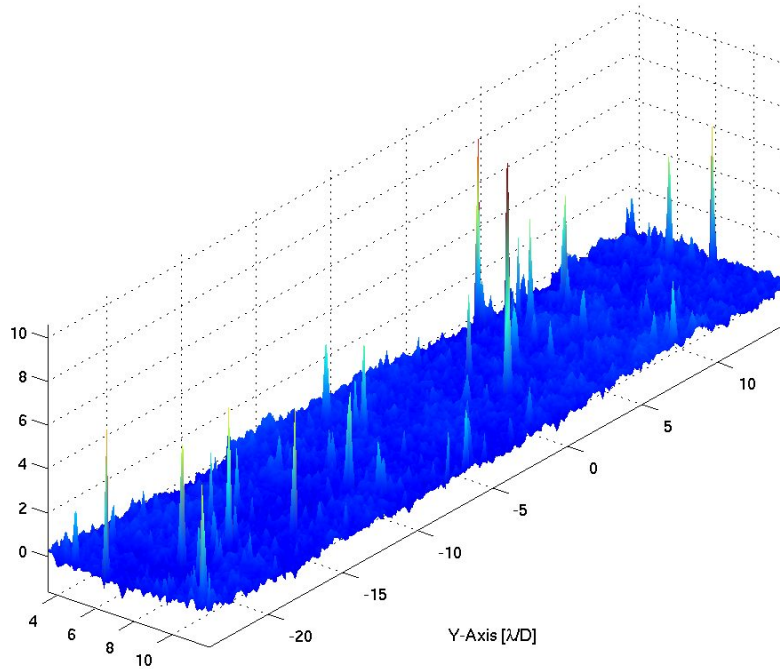


Figure 14. Values of the spot OD in the dark-hole side of the occulter. The OD value is multiplied by 50 for a better visibility.

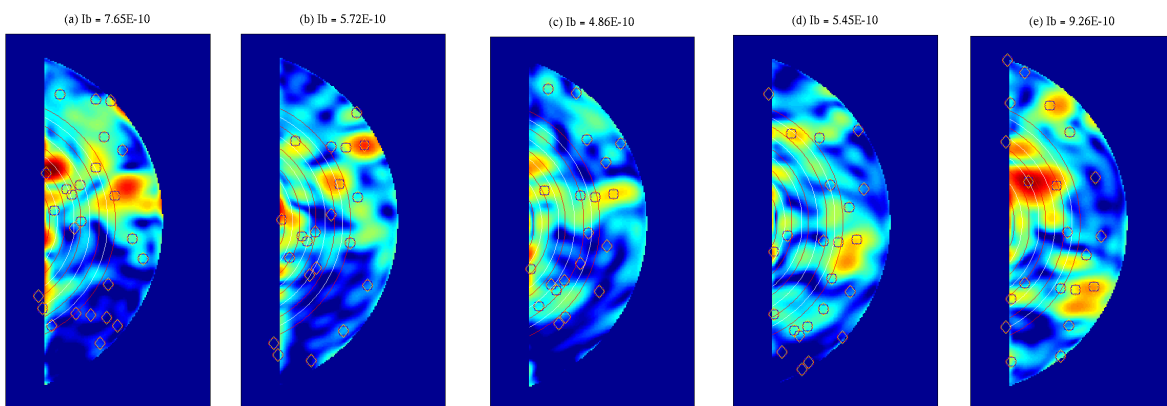


Figure 15. Change in $I_n(x, y)$ map when the Occulter is moved downward in a step of $\sim 21\mu\text{m}$. The red and the white arc lines indicate the positions of the Airy-ring peaks and valleys at the occulter plane. The markers indicate the locations of the major occulter spots.

Figures 15(a-e) show the after-control 10%-broadband $I_n(x, y)$ maps corresponding to 5 different locations when the occulter is moved downward in an increment of $\sim 21\mu\text{m}$. We used $F_{\text{spot}} = 1$ in these simulations. The red- and the white-circular lines indicate the locations of the peaks and the valleys of the Airy-rings at the occulter plane, and the markers indicate the locations of the major measured particles (or low transmission areas) on the occulter. Given in each sub-plot title is the corresponding I_b -value. We found that the contrast map features do not track in a predictable way as the occulter is moved downward. This means that it is meaningless to associate the colored-features of the

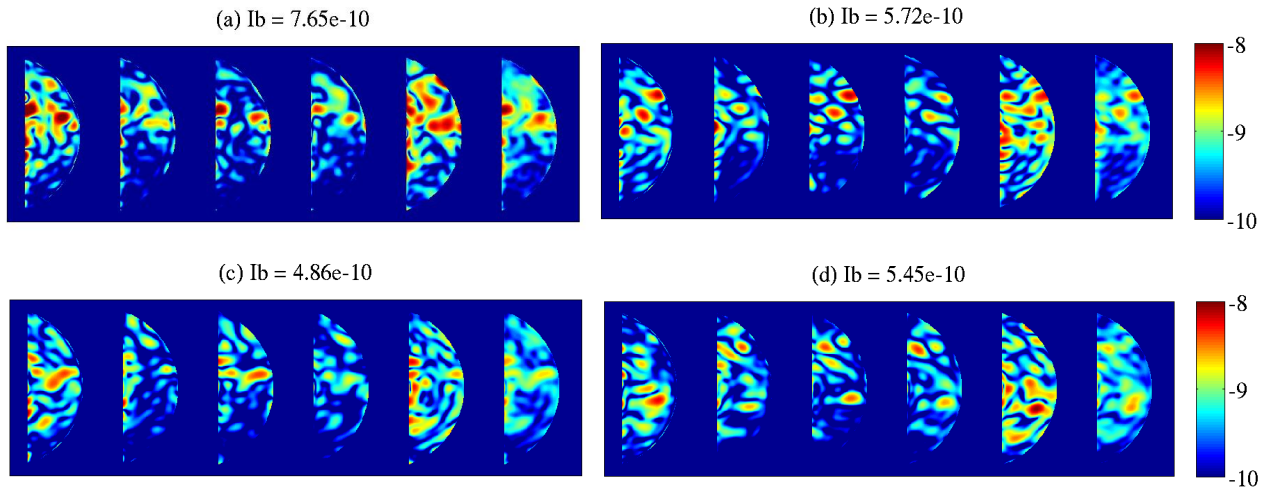


Figure 16. Simulated $I_n(x, y)$ maps corresponding to 4 different occulter positions. The occulter positions are the same as those used to obtain the first 4 broadband $I_n(x, y)$ maps in Fig. 15. As in Figs. 1(a-b), the leftmost images in each frame are for $\lambda = 768, 784, 800, 816,$ and 832nm , respectively, and the rightmost images are their mean representing the 10% broadband $I_n(x, y)$ map.

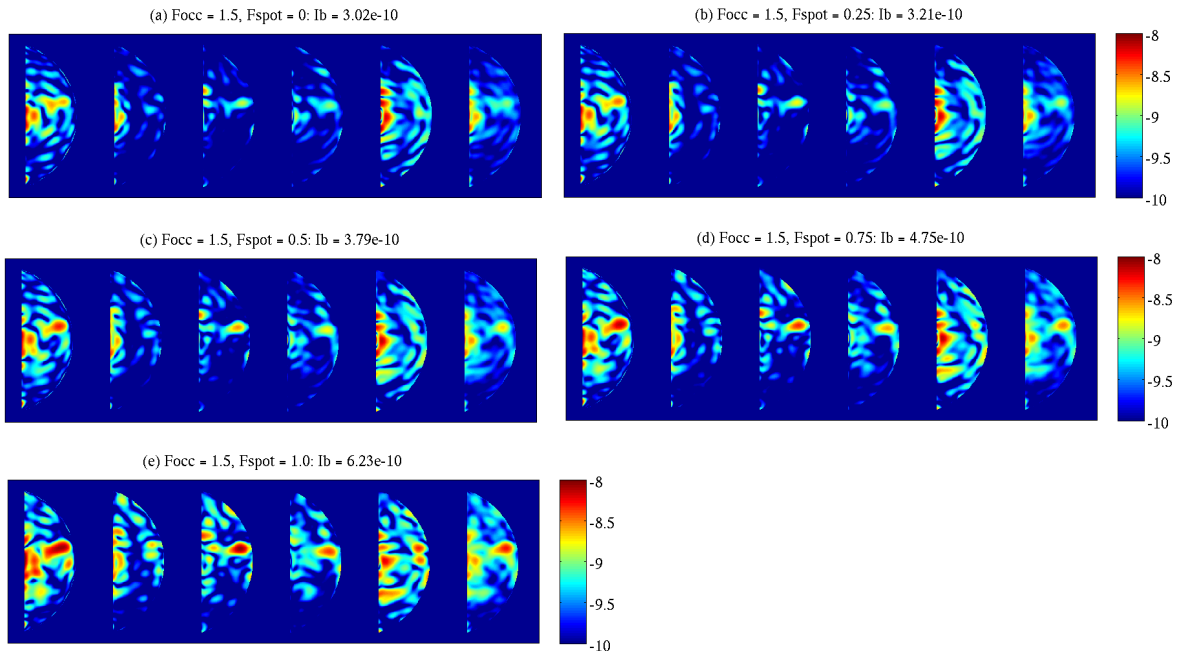


Figure 17. Simulated $I_n(x, y)$ maps similar to Fig. 16(c), except that the parasitic occulter is multiplied by $\times 1.5$ ($F_{\text{occ}} = 1.5$), and F_{spot} is varied from 0 to 1.0 with an increment of 0.25.

measured contrast maps with the locations of the actual spots of the occulter. This is one of the most important findings of this study. Figures 16(a-d) show the individual and the averaged after-control $I_n(x, y)$ maps corresponding to Figs. 15(a-d). We can see that both the I_b -values and the $I_n(x, y)$ map features of these simulated results are comparable to the measured data. However, we did not find a mask position where the measured speckles resemble one-for-one the model speckles.

Figures 17(a-e) are the same as Fig. 16(c) except that we multiplied the parasitic occulter phase by $\times 1.5$ ($F_{\text{occ}} = 1.5$) and varied F_{spot} from 0 to 1.0 with an increment of 0.25. That is, a fairly big range of spot phases can yield I_b -values that are within a factor of 2 of the measured I_b -value.

5. CONCLUSION

We have shown that the observed contrast performance of our HCIT testbed cannot be predicted by introducing certain defects to the occulter OD profile, such as reducing the maximum OD value, making the OD profile asymmetric, or by skewing the OD profile. Neither can it be predicted by increasing the parasitic phase of the occulter. These kinds of changes in occulter characteristics still preserve the fairly regularly spaced Airy-ring pattern of the final focal-plane PSF, which is something not observed in the measured data. These findings indicate that the Lyot coronagraph design implemented on the HCIT is fairly tolerant to fabrication errors in the OD profile and the phase of the occulter. We found two kinds of situations where the predicted contrast maps become comparable to the measured data in terms of the mean contrast value and the contrast map features. They are: (1) When we introduce randomly distributed opaque spots having widths of $\sim 2.5\mu\text{m}$ to occulter transmission amplitude function. (2) When we use the measured occulter transmittance image with actual spots on it and after introducing additional phase values to all major occulter spots. Both of these conditions are possible in the real world, but we did not carry out an exhaustive study to find an exact match between the measured data and our prediction.

Our work suggests that the observed “hot spots” on the contrast maps cannot be predicted based on the actual locations of the occulter spots unless the occulter spot is fairly large, such as in Figs. 9(a-b) of Ref. [7], where an occulter spot leads to $I_b > 10^{-8}$. That is because the “hot spots” on the contrast maps are a delicate function of the EFC algorithm and possibly a function of the interaction between the spots and the incident Airy rings.

In future work we will report on model and data agreement for different wavelength control bandwidths, non-functional DM actuators, and the ability to discriminate instrument-induced speckles from other background sources. These experimental validations of key coronagraph sensitivity factors will additionally contribute to the confidence in performance prediction models for future flight systems.

This work was carried out at the Jet Propulsion Laboratory, California Institute of Technology, under contract with the National Aeronautics and Space Administration. Funding was provided through the 2010 Technology Demonstrations for Exoplanet Missions (TDEM) Strategic Astrophysics Technology proposal.

REFERENCES

- [1] John T. Trauger, Chris Burrows, Brian Gordon, Joseph J. Green, Andrew E. Lowman, Dwight Moody, Albert F. Niessner, Fang Shi, and Daniel Wilson, “Coronagraph contrast demonstrations with the high-contrast imaging testbed,” *Proc. SPIE*, **5487**, 1330 (2004).
- [2] Andrew E. Lowman, John T. Trauger, Brian Gordon, Joseph J. Green, Dwight Moody, Albert F. Niessner, and Fang Shi, “High-contrast imaging testbed for the Terrestrial Planet Finder coronagraph,” *Proc. SPIE*, **5487**, 1246 (2004).
- [3] Erkin Sidick, Fang Shi, Scott Basinger, Dwight Moody, Andrew E. Lowman, Andreas C. Kuhnert, and John T. Trauger, “Performance of TPF’s High-Contrast Imaging Testbed: Modeling and simulations,” *Proc. SPIE*, **6265**, 62653L (2006).
- [4] Amir Give’on *et al*, “Broadband wavefront correction algorithm for high-contrast imaging system,” *Proc. SPIE*, **6691**, 66910A (2007).

- [5] *Modeling and Analysis for Controlled Optical Systems User's Manual*, Jet Propulsion Laboratory, California Institute of Technology, Pasadena, CA.
- [6] Erkin Sidick, Stuart Shaklan, Amir Give'on, and Brian Kern, "Studies of the effects of optical system errors on the HCIT contrast performance," *Proc. SPIE*, **8151**, 8151-06 (2011).
- [7] Erkin Sidick, Stuart Shaklan, John Krist, Eric J. Cady, and Brian Kern, "HCIT contrast performance sensitivity studies: Simulation versus experiment," *Proc. SPIE*, vol. 8864, pp. 8864Q-1 (2013).
- [8] Erkin Sidick, Stuart Shaklan, and Kunjithapatham Balasubramanian, "HCIT Broadband Contrast Performance Sensitivity Studies," *Proc. SPIE*, 8520, 85200M-1 (2012).
- [9] D. C. Moody and J. T. Trauger, "Hybrid Lyot coronagraph masks and wavefront control for improved spectral bandwidth and throughput," *Proc. SPIE*, 6693, 66931I-9 (2007).
- [10] "Exoplanet Exploration Coronagraph Technology: Technology Milestone #2 Report," Brian Kern, Andreas Kuhnert and John Trauger, editors, 8 Aug. 2008, <http://exep.jpl.nasa.gov/TPF-C/HCIT-Milestone2Signed-2008-08-08.pdf>.
- [11] K. Balasubramanian, "Band-limited image plane masks for the Terrestrial Planet Finder coronagraph: materials and designs for broadband performance," *Appl. Opt.* 47, pp.116-125 (2008).